Bending springback behavior related to deformation-induced phase transformations in Ti–12Cr and Ti–29Nb–13Ta–4.6Zr alloys for spinal fixation applications

Huihong Liu[a,*], Mitsuo Niinomi[b], Masaaki Nakai[b], Junko Hieda[b], Ken Cho[b]

[a]*Graduate Student, Department of Materials Science, Graduate School of Engineering, Tohoku University, Sendai 980-8579, Japan*

[b]*Institute for Materials Research, Tohoku University, Sendai 980-8577, Japan*

∗ Corresponding author:

Huihong Liu

Department of Materials Science, Graduate School of Engineering, Tohoku University, 6-6 Aoba, Aramaki, Aoba-ku, Sendai 980-8579, Japan

Tel.: +81-22-215-2390

Fax: +81-22-215-2553

E-mail: liuhuihong@imr.tohoku.ac.jp

Abstract

The springback behavior of Ti–12Cr and Ti–29Nb–13Ta–4.6Zr (TNTZ) during deformation by bending was investigated; and the microstructures of the non-deformed and deformed parts of both alloys were systematically examined to clarify the relationship between microstructure and springback behavior.

For the deformed Ti–12Cr alloy, deformation-induced ω-phase transformation occurs in both the areas of compression and tension within the deformed part, which increases the Young's modulus. With the deformed TNTZ alloy, deformation-induced ω-phase transformation is observed in the area of compression within the deformed part; while a deformation-induced α″ martensite

© 2014. This manuscript version is made available under the Elsevier user license
http://www.elsevier.com/open-access/userlicense/1.0/

transformation occurs in the area under tension, which is likely to be associated with the pseudoelasticity of TNTZ. Among these two alloys, Ti–12Cr exhibits a smaller springback and a much greater bending strength when compared with TNTZ; making Ti–12Cr the more advantageous for spinal fixation applications.

1. Introduction

With the increasing risk of the population of aged people experiencing a hard tissue failure, there is an increasing demand for metallic biomaterials that are suitable for replacing failed hard tissue (Niinomi, 2003). Examples of practical metallic biomaterials include various stainless steels, cobalt (Co)-chromium (Cr) alloys, and titanium (Ti) and its alloys (Niinomi et al., 2012). Among these, titanium and its alloys exhibit excellent specific strength and balance of mechanical properties, good corrosion resistance, and the best biocompatibility of all metallic biomaterials. They are not, surprisingly therefore, receiving increasing attention for a wide range of biomedical applications (Miura et al., 2011; Semlitsch, 1986; Wang, 1996). Up to now, pure titanium and Ti–6Al–4V alloy have been the most widely used Ti-biomaterials; however, some disadvantages to their use have been identified. Pure titanium only possesses moderate mechanical properties (Niinomi, 1998); while the toxicity of vanadium (V) (Domingo, 2002) and neurotoxicity of aluminum (V) (Boyce et al., 1992) in Ti64 poses a risk to safety with long-term implantation. Moreover, the Young's moduli of pure titanium (~105 GPa) and Ti64 (~110 GPa) (Niinomi, 2003; Pilliar, 1991) are still much higher than that of the human bone (~10-30 GPa) (Niinomi et al., 2012), with this mismatch in Young's modulus introducing a stress-shielding effect that leads to bone absorption (Sumitomo et al., 2008).

In light of these issues, a novel β-type titanium alloy composed of non-toxic and allergy-free elements (Ti–29Nb–13Ta–4.6Zr mass%, hereafter abbreviated as TNTZ), has been developed by Niinomi et al. based on the d-electron design method (Kuroda et al., 1998). This alloy exhibits excellent corrosion resistance and biocompatibility, with a low Young's modulus (~60 GPa). It has therefore been investigated for use in many practical applications, such as the production of implant

rods for spinal fixture (Tamura et al., 2007). In spinal fixation, the low Young's modulus and excellent biocompatibility of TNTZ is beneficial for patients; however, this alloy possesses only relatively moderate mechanical properties (ultimate tensile strength=~510 MPa) (Kuroda et al., 1998) which are inadequate for practical application. On the other hand, according to surgeons specializing in spinal diseases, the implant rod should exhibit a small degree of springback so that it can offer greater handling ability for surgeons who are required to bend the rod to conform to the curvature of the spine within a limited space inside the patient's body (Steib et al., 2004). As we know, the amount of springback is decided by both the strength and the Young's modulus. Given the same strength, it is the rod with the higher Young's modulus that will exhibit the smaller springback; that is, a high Young's modulus is preferable to suppress springback from the viewpoint of surgeons. There is therefore a conflicting requirement in Young's modulus from the point of view of the patients and the surgeons, which cannot be fully satisfied by TNTZ.

Recently, a number of researchers (Liu et al., 2013; Nakai et al., 2011; Zhao et al., 2012a, 2012b; Zhao et al., 2011) have focused on the development of new β-type titanium alloys in order to solve this problem; such as Ti–30Zr–3Cr–3Mo, Ti–17Mo, and Ti–12Cr. These alloys possess a novel property called "changeable Young's modulus"; in which a high Young's modulus can be obtained for the deformed part of the materials, while the Young's modulus of the non-deformed part remains low. This is made possible by deformation-induced ω-phase transformation localized within the deformed part of the material and provides an opportunity to satisfy the conflicting requirement between patients and surgeons. Among these novel alloys, Ti–12Cr (Zhao et al., 2012a) demonstrates a great change in Young's modulus; while also exhibiting a high tensile strength, acceptable elongation, and a high cytocompatibility. It is therefore considered to be a suitable potential candidate for spinal fixation applications.

The effect of a changeable Young's modulus on springback has previously been investigated by tensile loading-unloading tests in Ti–12Cr and TNTZ (Zhao et al., 2012a). However, as mentioned above, the implant rods will be deformed by bending during surgery. Bending is therefore under much more complex stress conditions than a tensile test, as both compressive and tensile stresses are loaded on the inside and outside of the deformed part, respectively. Furthermore, these bending stresses gradually increase from the center to the surface of both sides during bending. This creates a need to investigate the springback behavior of materials during bending, with this study focusing on the behavior of Ti–12Cr and TNTZ. The microstructures of the bent parts were also systematically examined in order to clarify the relationship between the springback behavior and microstructure.

2. Experimental procedures

2.1. Material preparation

An ingot of Ti–12Cr (mass%) alloy was prepared by levitation melting under a high-purity argon atmosphere. The ingot was hot forged at 1173 K in an argon atmosphere into a bar with a diameter of 25mm, and then air cooled. A hot forged bar of TNTZ with a diameter of 25mm was received for comparison. Both bars were hot rolled at 1273 K under an argon atmosphere into rods with a diameter of 7mm, which were then subjected to air cooling. The cooled rods of Ti–12Cr and TNTZ were solution treated for 3.6ks under vacuum at 1123 K and 1063 K, respectively, and then rapidly quenched in ice-water. Finally, both of the solution treated rods were subjected to turning to remove oxide layers, with the final rod obtained having a diameter of 5 mm. Prior to deformation by bending, the microstructures of both the Ti–12Cr and TNTZ alloys consisted of equiaxed β grains.

2.2. Evaluation of springback properties

The springback properties of the prepared alloys were evaluated at room temperature by three-point bending loading–unloading tests using an Instron-type machine (Shimadzu AGS-20kNG) at a cross-head speed of 8.33×10^{-6} m s^{-1}. Rod specimens with a diameter of 5 mm and a length of 50 mm were cut from the prepared rods, with the bending loading-unloading procedures shown in Fig. 1. The distance between the two parallel supports for the specimens was 30 mm. The specimens were bent under loading until a certain deflection was achieved, which was then followed by unloading. Bending loading-unloading tests were conducted with deflections of 3.0, 4.0, and 5.0 mm.

2.3. Microstructural analysis

The microstructures of the non-deformed and deformed parts of the bent specimens were observed from cross sections. In the deformed parts, different areas of the cross section were subjected to different stress conditions; that is the top area was compressed, the center area was non-deformed, and the bottom area was in tension (as illustrated in Fig. 2a-b). The amount of the compressive and tensile deformation is approximately estimated in terms of quantitative strain for easy understanding. The bent specimen curvature is considered approximately as a circular arc. The geometrical relationship between the bent and original specimen curvatures is shown in Fig. 2c. It is known that the d is the deflection achieved in the bending test before unloading (3 mm, 4 mm and 5 mm), while the L is the half distance between two parallel supports for the specimen (15 mm); thus the radius of the bent curvature, R, can be obtained. A magnification of the area labeled by the dotted rectangular block is exhibited in Fig. 2d. It shows that the area above the neutral axis, where there is no strain, is compressed while the area below is in tension after bending. The bending strain, ε, at any location, taking an example as location (a′-b′), can be calculated according to the equation (Gere and Goodno, 2012):

$$\varepsilon = -y/R \quad (1)$$

in which y is the distance apart from the neutral axis and R is the radius of the bent curvature. Therefore, the bending strain increased proportionally from the neutral axis to the surface, and the maximum compressive strain and tensile strain were achieved in the location (A′-B′) and (C′-D′), respectively. As the diameter of the rod is given as 5 mm, thus, in the bending tests with deflections of 3 mm, 4 mm and 5 mm, the maximum compressive strain obtained in the compression areas were approximately -6.4%, -8.3% and -10%, respectively, while the maximum tensile strain achieved in the tension areas were closely 6.4%, 8.3% and 10%, respectively.

The microstructures of each of these three areas, including compression area, non-deformed area and tension area, were analyzed systematically. The phase compositions of all the specimens were identified by X-ray diffraction (XRD), using a Bruker D8 Discover 2D X-ray diffractometer with Cu Kα radiation at a voltage of 40 kV and a current of 40 mA. The microstructures were examined by optical microscopy (OM) (Olympus BX51), electron backscattered diffraction (EBSD) (Quanta 200 3D SEM-TSL), and transmission electron microscopy (TEM) (JEOL JEM-2000EX). For the OM and EBSD observations, the specimens were mechanically polished using SiC waterproof emery paper of up to 2400 grit and a colloidal SiO_2 suspension. The mirror-polished specimens of Ti–12Cr were etched with aqueous solutions of hydrofluoric acid (HF: 1 vol%) and nitric acid (HNO_3: 0.5 vol%) for 1 min, while the specimens of TNTZ were etched with hydrofluoric acid (HF: 5 vol%) for 10 min. For TEM observations, the specimens were first mechanically polished to a thickness of ~40 μm, and then dimpled to a thickness of ~10 μm with a phosphor bronze ring. Finally, the specimens were ion milled to a thin foil. TEM observations were conducted at an accelerating voltage of 200 kV.

3. Results and discussion

3.1. Springback properties

Figure 3 shows the stress-deflection curves of Ti–12Cr and TNTZ from three point bending loading-unloading tests with deflections of 3.0 4.0, and 5.0 mm and schematic illustration of springback, loading slope and unloading slope in a stress-deflection curve for clear understanding each factor on the stress-deflection curves. For TNTZ, the deflection value corresponding to a stress of zero after unloading from a deflection of 3.00 mm is ~2.00 mm; making the recovery deflection value ~1.00 mm. However, under the same conditions the recovery deflection value of Ti–12Cr is less at ~0.90 mm. Similar results were obtained in tests with deflections of 4.00 and 5.00 mm; with the respective recovery deflection values of ~0.94 and ~0.98 for Ti–12Cr less than the ~1.03 and ~1.08 with TNTZ. This means that Ti–12Cr exhibits a smaller springback than TNTZ. Furthermore, Ti–12Cr also exhibits much higher bending strength than TNTZ that is advantageous for practical applications. Generally speaking, materials with higher strength have a greater ability to retain their shape after being manipulated to a fixed form. Furthermore, a greater strength allows for devices to be smaller in size while still maintaining the same force after surgical spinal fixture. Consequently, in terms of both springback and strength, Ti–12Cr is far better suited to spinal fixation applications than TNTZ.

The slopes of the loading and unloading curves of Ti–12Cr and TNTZ, which are related to the Young's moduli of the alloys, are shown in Fig. 3. It is worth noting that the unloading slope of Ti–12Cr is larger than loading slope in each experiment; while the unloading slope of TNTZ is nonlinear, decreasing in value compared to the loading slope during recovery.

3.2. Microstructures

Since similar springback and microstructure properties were obtained with Ti–12Cr and TNTZ subjected to the tests of varying deflection, only the microstructures of these two alloys after

subjection to a 4.00 mm deflection test are shown in this study.

3.2.1. Microstructure of Ti–12Cr after deformation by bending

Figure 4 shows optical micrographs and corresponding XRD profiles of non-deformed and deformed parts of Ti–12Cr subjected to deformation by bending. In the non-deformed part, the microstructure comprises equiaxed grains of a single β phase with a grain size of approximately 250 μm. Following deformation, lentoid structures are observed inside these equiaxed grains in both the compression (top) area and tension (bottom) area, while no structures other than equiaxed grains are observed in the non-deformed (center) area. The corresponding XRD profiles indicate that only those peaks related to the β phase are detected in all three areas.

To identify the lentoid structures, the deformed part of Ti–12Cr was further analyzed by EBSD. Figure 5 shows the EBSD results of the tension area, with lentoid structures evident in the orientation image maps owing to their difference in color to the matrix (Fig. 5a). Combined with the XRD results, this indicates that the crystallographic orientations of the lentoid structures differ from those of the matrix. The misorientation as a function of distance was measured across the lentoid structures (as indicated by the arrow in Fig. 5a), revealing that the misorientation between the lentoid structures and the matrix is approximately 10°. These results also show that the lentoid structures contain several regions with different crystal orientations, including both continuous and discontinuous crystal rotations. In the corresponding grain boundary maps (Fig. 5b), the red lines correspond to the boundaries of most of the lentoid structures, which suggests they have a misorientation angle of ~10° around the <110>β direction. These results indicate that the lentoid structures are relatively far from the {332}<113> mechanical twinning of Ti, which has a misorientation angle of ~50.5° around the <110>β direction (Bertrand et al., 2011; Furuta et al., 2005; Hanada and Izumi, 1987; Hanada et al., 1985). These characteristics of the lentoid structures

correspond to a particular kind of deformation band, called the kink band (Yang et al., 2010). These apparent kink bands are observed in both the tension and compression areas of the bent Ti–12Cr samples.

Figure 6 shows the TEM results of the non-deformed and deformed parts of bent Ti–12Cr. For the non-deformed part, only spots corresponding to the β phase were detected in the electron diffraction pattern of the [110]β zone (Fig. 6a). This indicates that the non-deformed part of Ti–12Cr consists of a single β phase, which is consistent with the OM and XRD results. However, for the deformed part, the electron diffraction pattern of the compression area shows β spots in combination with additional spots related to the ω phase (Figs. 6b and c). In addition, a single variant {211}<111> plate-like ω phase was observed in the tension area from the electron diffraction pattern and corresponding dark field image (Figs. 6d-f). These results suggest that deformation-induced ω-phase transformation occurs in both the compression and tension areas of bent Ti–12Cr.

3.2.2. Microstructure of TNTZ after deformation by bending

Optical micrographs and corresponding XRD profiles of non-deformed and deformed parts of TNTZ subjected to deformation by bending are shown in Fig. 7. The microstructure of non-deformed part consists of equiaxed β grains with a grain size of around 80 μm. After deformation, a large area of band structure with a width of ~3 μm is formed in the equiaxed grains in both the compression (top) and tension (bottom) area; while no obvious change in microstructure can be observed in the non-deformed (center) area. According to the corresponding XRD profiles, β peaks in combination with peaks derived from the α″ phase are detected in the tension area, while weak ω peaks in addition to β peaks are observed in the compression area. For the non-deformed area, the XRD profile exhibits α″ peaks, weak ω peaks in addition to β peaks. This latter

observation is due to the detecting area overlapping parts of the compression and tension areas.

The deformed part of TNTZ was further examined by EBSD, in order to clarify the nature of the band structures. Figure 8 shows the EBSD results of the tension area of bent TNTZ, with band structures observable in the orientation image map (Fig. 8a). According to the misorientation as a function of distance (Fig. 8c), in the direction indicated by the arrow seen in the orientation image map and corresponding grain boundary maps (Fig. 8b), the misorientation between the band structures and the matrix around the <110>β direction is shown to be ~50.5°. These band structures are therefore delineated as {332}<113> mechanical twinning, based on the view that {332}<113> mechanical twinning has a misorientation angle of ~50.5° around the <110>β direction (Bertrand et al., 2011; Furuta et al., 2005; Hanada and Izumi, 1987; Hanada et al., 1985). Such mechanical twinning could be observed in both the tension and compression areas of bent TNTZ.

The non-deformed and deformed parts of bent TNTZ were also observed by TEM, with the results shown in Fig. 9. The selected area electron diffraction pattern shows that only β phase is present in the non-deformed part (Fig. 9a). In the deformed part on the other hand, a band structure with a width of ~3 μm is observed in the compression area, as shown in the Figs. 9b-d. This band structure is defined as {332}<113> mechanical twinning according to the electron diffraction pattern, which is consistent with the OM and EBSD results. Furthermore, a plate-like single variant ω phase was observed in the compression area (Fig. 9e-g), suggesting the occurrence of deformation-induced ω-phase transformation. For the tension area, a deformation-induced α″ martensite was observed, as shown in Fig. 9h-i. These results again show good consistency with the XRD results.

3.3. Discussion

It has been determined that the mechanism of plastic deformation in Ti alloys changes from

twinning to dislocation glide with increasing stability of the β phase (Kuroda et al., 1998; Yang et al., 2010). Li et al. (Li et al., 2013) also reported that with an increase in β phase stability, the deformation-induced phase transformation changes from α″ martensite transformation to ω transformation. In this study, the deformation mechanism of TNTZ was found to include mechanical twinning, deformation-induced α″ martensite transformation, and deformation-induced ω transformation; while the deformation mode of Ti–12Cr is likely to be a combination of dislocation slip, kink bands (kinking is a type of cooperative deformation mode (Sakai et al., 2009; Yang et al., 2010)) and deformation-induced ω transformation. Molybdenum equivalence (Mo_{eq}) is typically used to evaluate the β phase stability in Ti alloys and is determined by the Mo_{eq} equation (Boyer et al., 1994). The Mo_{eq} of TNTZ is ~10.65 and is less than that of Ti–12Cr (~15), which indicates that the β phase stability is lower in TNTZ than in Ti–12Cr. Therefore, the trend of deformation mode change with increasing β phase stability in TNTZ and Ti–12Cr is consistent with the literature.

In the deformed Ti–12Cr, deformation-induced ω-phase transformation occurs in both the compression and tension areas; however, the deformation-induced ω-phase transformation and α″ martensite transformation occur in the compression and tension areas of bent TNTZ, respectively. It has been reported (Bhattacharjee et al., 2005; Duerig et al., 1982) that while the metastable β phase has a body-centered cubic (bcc) structure, the atoms in orthorhombic α″ are positioned at (0, 0, 0), (*a*/2, *b*/2, 0), (0, 2*b*/3, c/2), and (*a*/2, *b*/6, *c*/2). The lattice correspondence between β and α″ phases is therefore shown by the following: [100]β//[100]α″; (011)β//(010)α″. The lattice parameters of the orthorhombic martensite cell in Ti–10V–2Fe–3Al have been previously obtained as *a*=0.301 nm, *b*=0.483 nm, and *c*=0.462 nm, while the retained β phase has a lattice parameter of 0.324 nm. Consequently, the β to α″ martensite transformation in Ti–10V–2Fe–3Al is accompanied

by lattice strain in the three principal lattice directions of: ε_1= -7.1 %, ε_2= +7.2 %, and ε_3= +1.1 % (Bhattacharjee et al., 2005; Duerig et al., 1982). This indicates that during the β to α″ martensite transformation, the [100]β direction should undergo a negative strain (ε_1= -7.1 %), with a positive strain (ε_2= +7.2 %) occurring in the [110]β direction in order to form orthorhombic α″. Typically, the received TNTZ rod had a [110]β texture along its axis. This result was confirmed by the XRD results, in which (110)β peaks with an extremely high intensity and weak β peaks of other lattice plane indexes were detected. Therefore, in deformed TNTZ the α″ martensite expansion along ε_2 ([010] α″//[110]β) is stabilized by a tensile stress along the axis of the rod; and so deformation-induced α″ martensite transformation occurs in the tension area. As previously reported (Banerjee and Mukhopadhyay, 2007), the formation of the ω phase involves an athermal mechanism known as lattice collapse; that is, the ω lattice can be derived by collapsing a pair of neighboring (111) planes in a β-bcc lattice via atomic shuffling into the intermediate position. As a result, it is apparent that the ω lattice has a higher intensity structure than that of the bcc β lattice. From the structural viewpoint of these two phases, the presence of internal compressive stress in a crystal is reasonably presumed to promote the ω phase transformation (Ezaki et al., 1991). Furthermore, it has been reported that the β to ω phase transformation could potentially occur in β-type Ti–Mo alloys along the {112}<111> twin boundary, where compressive stress occurs (Sukedai et al., 2011). Therefore, the occurrence of deformation-induced ω-phase transformation in the compression area of deformed TNTZ can be understood on the basis of these previous results.

It is well known that the mechanical properties of materials have a great dependence on the microstructure. In the deformed Ti–12Cr, the deformation-induced ω-phase formed in the compression and tension areas increases the Young's modulus, due to the higher Young's modulus of the ω phase compared with the β phase. Therefore, the unloading slope of Ti–12Cr is found to be

larger than the loading slope. Meanwhile, even though there is also a deformation-induced ω-phase transformation in the compression area of the deformed TNTZ, a large amount of deformation-induced α″ martensite is also formed in the tension area. The authors (Niinomi et al., 2009) have previously reported that TNTZ shows a pseudoelastic deformation behavior during tensile loading-unloading test. This pseudoelasticity is likely to be related to the reversible α″ martensite transformation, which was mentioned in the previous research (Niinomi et al., 2009) and could be further readily presumed from the present study. TNTZ therefore exhibits a large springback owing to the combination of a low Young's modulus and pseudoelasticity.

4. Conclusions

In this study, the springback behaviors of Ti–12Cr and TNTZ during bending deformation were investigated. The microstructures of the non-deformed and deformed parts of both alloys were systematically examined in order to clarify the relationship between microstructure and springback behavior. From this, the following conclusions were obtained:

(1) {332}<113> mechanical twinning forms in TNTZ during bending deformation; while deformation bands, which appear to be kink bands rather than {332}<113> mechanical twinning, are observed in deformed Ti–12Cr. This difference is attributed to the higher stability of the β phase in Ti–12Cr.

(2) For the deformed Ti–12Cr, deformation-induced ω-phase transformation occurs in both the compression and tension areas. This increases the Young's modulus of the deformed part, thereby increasing the slope during the unloading of bending.

(3) For the deformed TNTZ, deformation-induced α″ martensite transformation occurs in the tension area, while deformation-induced ω-phase transformation is observed in the compression area. The pseudoelasticity of TNTZ is likely to be related to the

deformation-induced α″ martensite formation.

(4) Among these two alloys, Ti–12Cr exhibits a smaller springback and greater bending strength compared with TNTZ. Given that a combination of low springback and high strength is essential for the practical use, Ti–12Cr is considered to be the more desirable material for application in spinal fixtures.

Acknowledgements

This work was supported in part by the Industrial Technology Research Grant Program in 2009 from the New Energy and Industrial Technology Development Organization (NEDO), Adaptable and Seamless Technology Transfer Program through Target-driven R&D (A-STEP) from the Japan Science and Technology Agency (JST), and Grant-in-Aid for Scientific Research (A), Young Scientists (A), and Challenging Exploratory Research from the Japan Society for the Promotion of Science (JSPS), Japan.

References

Banerjee, S., Mukhopadhyay, P., 2007. Transformations Related to Omega Structures, in: Cahn, R.W. (Eds.), Phase Transformations: Examples from Titanium and Zirconium Alloys. Elsevier, Great Britain, pp. 474-508.

Bertrand, E., Castany, P., Peron, I., Gloriant, T., 2011. Twinning system selection in a metastable β-titanium alloy by Schmid factor analysis. Scripta Mater. 64, 1110-1113.

Bhattacharjee, A., Bhargava, S., Varma, V.K., Kamat, S.V., Gogia, A.K., 2005. Effect of β grain size on stress induced martensite transformation in β solution treated Ti-10V-2Fe-3Al alloy. Scripta. Mater. 53, 195-200.

Boyce, B.F., Byars, J., McWilliams, S., Mocan, M.Z., Elder, H.Y., Boyle, I.T., Junor, B.J., 1992. Histological and electron microprobe studies of mineralisation in aluminium-related osteomalacia. J. Clin. Pathol. 45, 502-508.

Boyer, R., Welsch, G., Collings, E.W., 1994. Materials properties handbook: titanium alloys. ASM International, Materials park, OH.

Domingo, J., 2002. Vanadium and tungsten derivatives as antidiabetic agents. Biol. Trace. Elem. Res. 88, 97-112.

Duerig, T.W., Albrecht, J., Richter, D., Fischer, P., 1982. Formation and reversion of stress induced martensite in Ti-10V-2Fe-3Al. Acta. Metall. 30, 2161-2172.

Ezaki, H., Morinaga, M., Kato, M., Yukawa, N., 1991. Electronic and atomic-size effects on the omega phase formation in transition-metal based B.C.C alloys. Acta. Metal. Mater. 39, 1755-1761.

Furuta, T., Kuramoto, S., Hwang, J.H., Nishino, K., Saito, T., 2005. Elastic deformation behavior of

multi-functional Ti-Nb-Ta-Zr-O alloys. Mater. Trans. 46, 3001-3007.

Gere, J.M., Goodno, B.J., 2012. Mechanics of meterials eighth ed. Cengage learning, Canada.

Hanada, S., Izumi, O., 1987. Correlation of tensile properties, deformation modes, and phase stability in commercial β-phase titanium alloys. Metall. Trans. A 18, 265-271.

Hanada, S., Ozeki, M., Izumi, O., 1985. Deformation characteristics in beta-phase Ti-Nb alloys. Metall. Trans. A 16, 789‑795.

Kuroda, D., Niinomi, M., Morinaga, M., Kato, Y., Yashiro, T., 1998. Design and mechanical properties of new β-type titanium alloys for implant materials. Mater. Sci. Eng. A 243, 244–249.

Li, Q., Niinomi, M., Hieda, J., Nakai, M., Cho, K., 2013. Deformation-induced ω phase in modified Ti-29Nb-13Ta-4.6Zr alloy by Cr addition. Acta. Biomater. 9, 8027-8035.

Liu, H.H., Niinomi, M., Nakai, M., Hieda, J., Cho, K., 2013. Deformation-induced changeable Young's modulus with high strength in β-type Ti–Cr–O alloys for spinal fixture. J. Mech. Behav. Biomed. In Press.

Miura, K., Yamada, N., Hanada, S., Jung, T.K., Itoi, E., 2011. The bone tissue compatibility of a new Ti–Nb–Sn alloy with a low Young’s modulus. Acta. Biomater. 7, 2320–2326.

Nakai, M., Niinomi, M., Zhao, X.F., Zhao, X.L., 2011. Self-adjustment of Young’s modulus in biomedical titanium alloys during orthopaedic operation. Mater. Lett. 65, 688-690.

Niinomi, M., Akahori, T., Nakai, M., Tsutsumi, H., 2009. Effects of thermomechanical treatments on pseudoelastic strain characteristics of Ti-29Nb-13Ta-4.6Zr for biomedical applications. Mater. Trans. 50, 1704-1712.

Niinomi, M., Nakai, M., Hieda, J., 2012. Development of new metallic alloys for biomedical applications. Acta. Biomater. 8, 3888-3903.

Niinomi, M., 1998. Mechanical properties of biomedical titanium alloys. Mater. Sci. Eng. A 243, 231-236.

Niinomi, M., 2003. Recent research and development in titanium alloys for biomedical applications and healthcare goods. Sci. Technol. Adv. Mater. 4, 445-454.

Pilliar, R.M., 1991. Modern metal processing for improved load-bearing surgical implants. Biomaterials. 12, 95-100.

Sakai, T., Miura, H., Yang, X., 2009. Ultrafine grain formation in face centered cubic metals during severe plastic deformation. Mater. Sci. Eng. A 499, 2-6.

Semlitsch, M., 1986. Classic and new titanium alloys for production of artificial hip joints. Titan. 2, 721–740.

Steib, J.P., Dumas, R., Mitton, D., Skalli, W., 2004. Surgical correction of scoliosis by in situ contouring. Spine. 29, 193-199.

Sukedai, E., Shimoda, M., Nishizawa, H., Nako, Y., 2011. Nucleation behaviour of β to ω phase transformations in β-type Ti-Mo alloys. Mater. Trans. 52, 324-330.

Sumitomo, N., Noritake, K., Hattori, T., Morikawa, K., Niwa, S., Sato, K., Niinomi, M., 2008. Experiment study on fracture fixation with low rigidity titanium alloy. J. Mater. Sci. 19, 1581-1586.

Tamura, T., Kozuka, S., Oribe, K., Nakai, M., Niinomi, M., 2007. Evaluation of Ti-Nb-Ta-Zr as New Medical Implants, in: Niinomi, M., Akiyama, S., Hagiwara, M., Ikeda, M., Maruyama, K. (Eds.), Ti-2007 Science and Technology. The Japan Institute of Metals, Sendai, pp. 1441-1444.

Wang, K., 1996. The use of titanium for medical applications in the USA. Mater. Sci. A 213, 134–137.

Yang, Y., Wu, S.Q., Li, G.P., Li, Y.L., Lu, Y.F., Yang, K., Ge, P., 2010. Evolution of deformation

mechanisms of Ti-22.4Nb-0.73Ta-2Zr-1.34O alloy during straining. Acta. Mater. 58, 2778-2787.

Zhao, X.F., Niinomi, M., Nakai, M., Hieda, J., Ishimoto, T., Nakano, T., 2012a. Optimization of Cr content of metastable β-type Ti-Cr alloys with changeable Young's modulus for spinal fixation applications. Acta. Biomater. 8, 2392-2400.

Zhao, X.F., Niinomi, M., Nakai, M., Hieda, J., 2012b. Beta type Ti-Mo alloys with changeable Young's modulus for spinal fixation applications. Acta. Biomater. 8, 1990-1997.

Zhao, X.L., Niinomi, M., Nakai, M., Miyamoto, G., Furuhara, T., 2011. Microstructures and mechanical properties of metastable Ti-30Zr-(Cr, Mo) alloys with changeable Young's modulus for spinal fixation applications. Acta. Biomater. 7, 3230-3236.

Figure captions

Fig. 1. Schematic illustration of three point bending loading-unloading test procedure.

Fig. 2. (a-b) Illustration of different stress condition areas in a bending deformed part; (c-d) estimation of the amount of deformation in terms of strain in a bending deformed part.

Fig. 3. (a) stress curves of Ti-12Cr and TNTZ via three point bending loading-unloading tests with deflections of 3.0 mm, 4.0 mm, and 5.0 mm, and (b) schematic illustration of springback, loading slope and unloading slope in a stress-deflection curve.

Fig. 4. Optical micrographs and XRD profiles of non-deformed and deformed parts of Ti-12Cr subjected to bending deformation (after bending test with 4 mm deflection).

Fig. 5. EBSD analysis of tension area of bending deformed Ti-12Cr (after bending test with 4 mm deflection): (a) local orientation image map (OIM), (b) grain boundary map showing boundaries with a misorientation of ~10°along the <110>β direction (red lines), (c) misorientations relative to the first point along black arrows in (a).

Fig. 6. TEM observations of (a) non-deformed and (b-f) deformed parts of bent Ti-12Cr (after bending test with 4 mm deflection): (a) selected area electron diffraction pattern (SAED) of non-deformed part; (b) bright field image of compression area; (c) SAED taken from part marked by circle in (b); (d) bright field image of tension area; (e) SAED taken from area labeled by circle in (d); (f) dark field

image corresponding to diffraction spot denoted by red circle in (e). The beam direction is parallel to [110] β direction.

Fig. 7. Optical micrographs and XRD profiles of non-deformed and deformed parts of TNTZ subjected to bending deformation (after bending test with 4 mm deflection).

Fig. 8. EBSD analysis of tension area of bending deformed TNTZ (after bending test with 4 mm deflection): (a) local orientation image map (OIM), (b) grain boundary map showing boundaries with a misorientation of ~50.5°along <110>β direction (green lines), (c) misorientations relative to the first point along black arrows in (a).

Fig. 9. TEM observations of non-deformed part (a), compression area (b-g) and tension area (h-j) of deformed part of bended TNTZ (after bending test with 4 mm deflection): (a) selected area electron diffraction pattern (SAED) of non-deformed part; (b) bright field image of compression area; (c) SAED taken from part marked by circle in (b); (d) corresponding key diagram; (e) bright field image of compression area; (f) selected area electron diffraction pattern (SAED) taken from part marked by circle in (e); (g) dark field image corresponding to diffraction spot denoted by circle in (f); (h) bright field image of tension area; (i) SAED taken from part marked by circle in (h); (j) dark field image corresponding to diffraction spot denoted by circle in (i). The beam direction is parallel to [110]β direction.

Figure revised

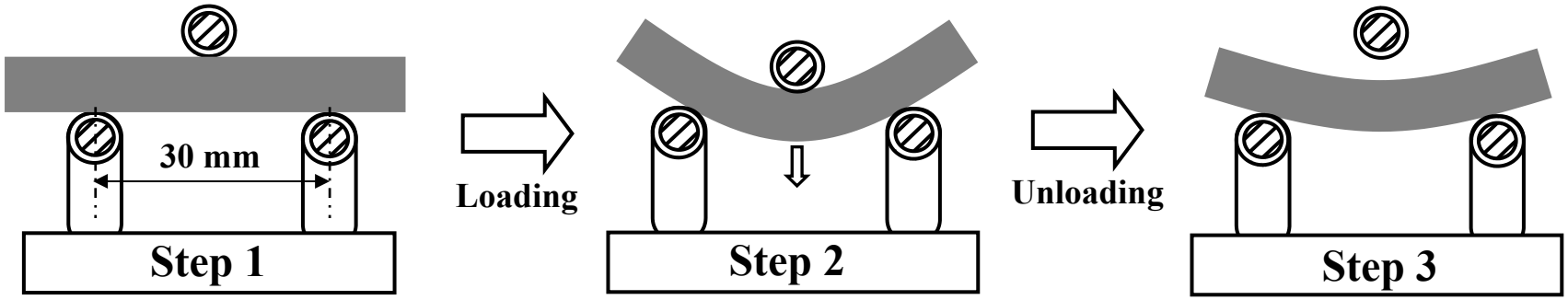

Fig. 1. Schematic illustration of three point bending loading-unloading test procedure.

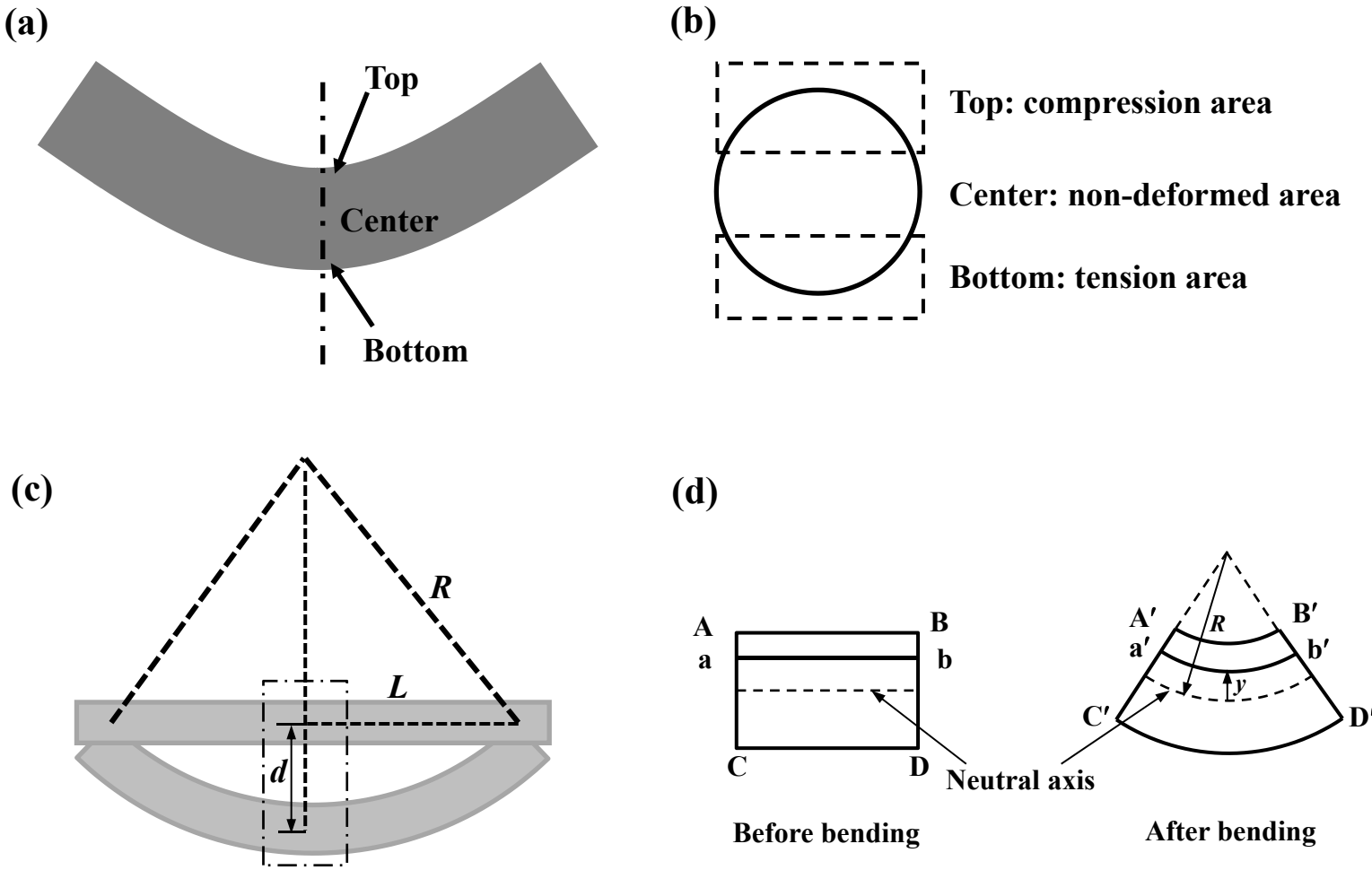

Fig. 2. (a-b) Illustration of different stress condition areas in a bending deformed part; (c-d) estimation of the amount of deformation in terms of strain in a bending deformed part.

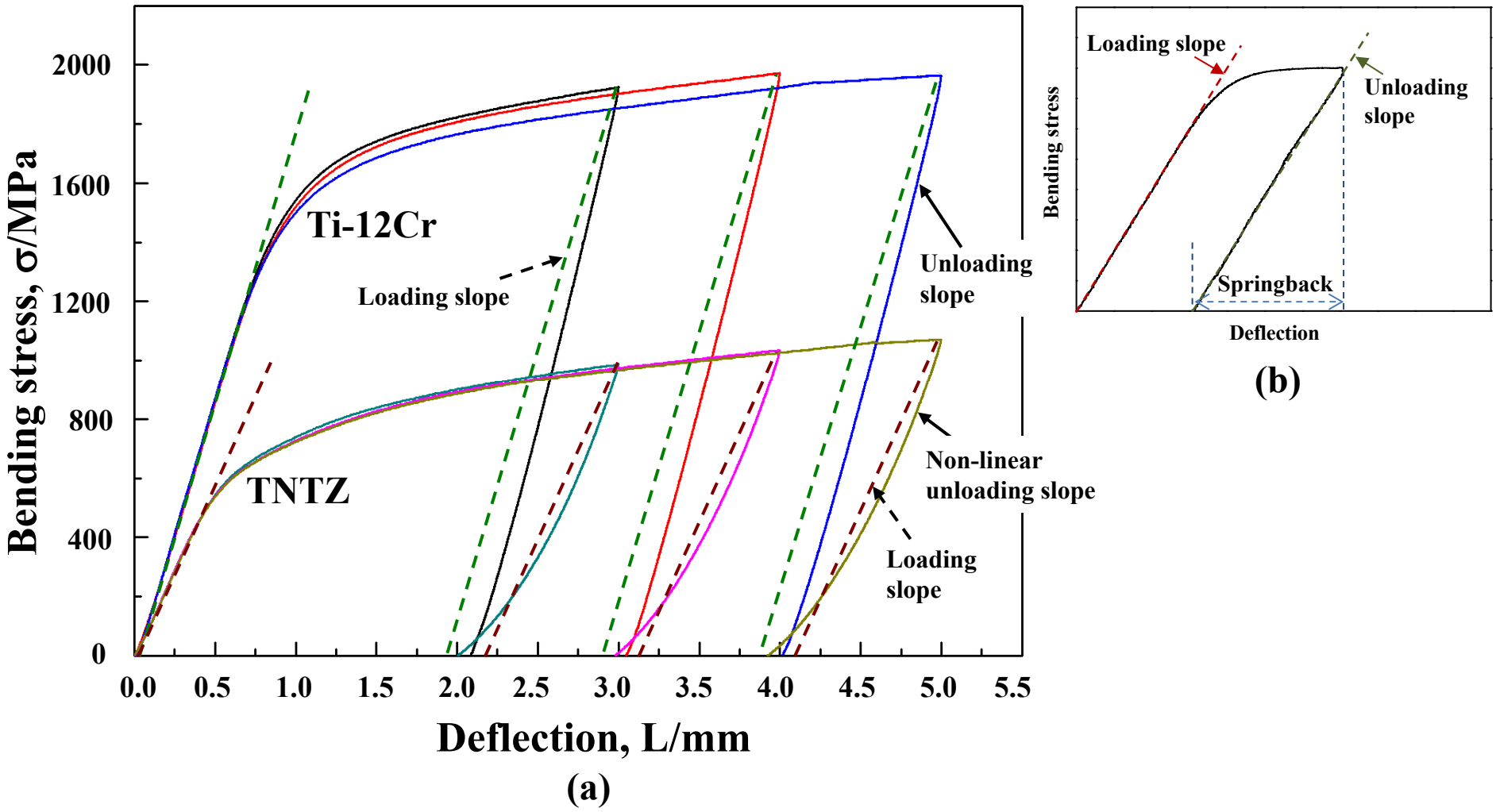

Fig. 3. (a) stress curves of Ti-12Cr and TNTZ via three point bending loading-unloading tests with deflections of 3.0 mm, 4.0 mm, and 5.0 mm, and (b) schematic illustration of springback, loading slope and unloading slope in a stress-deflection curve.

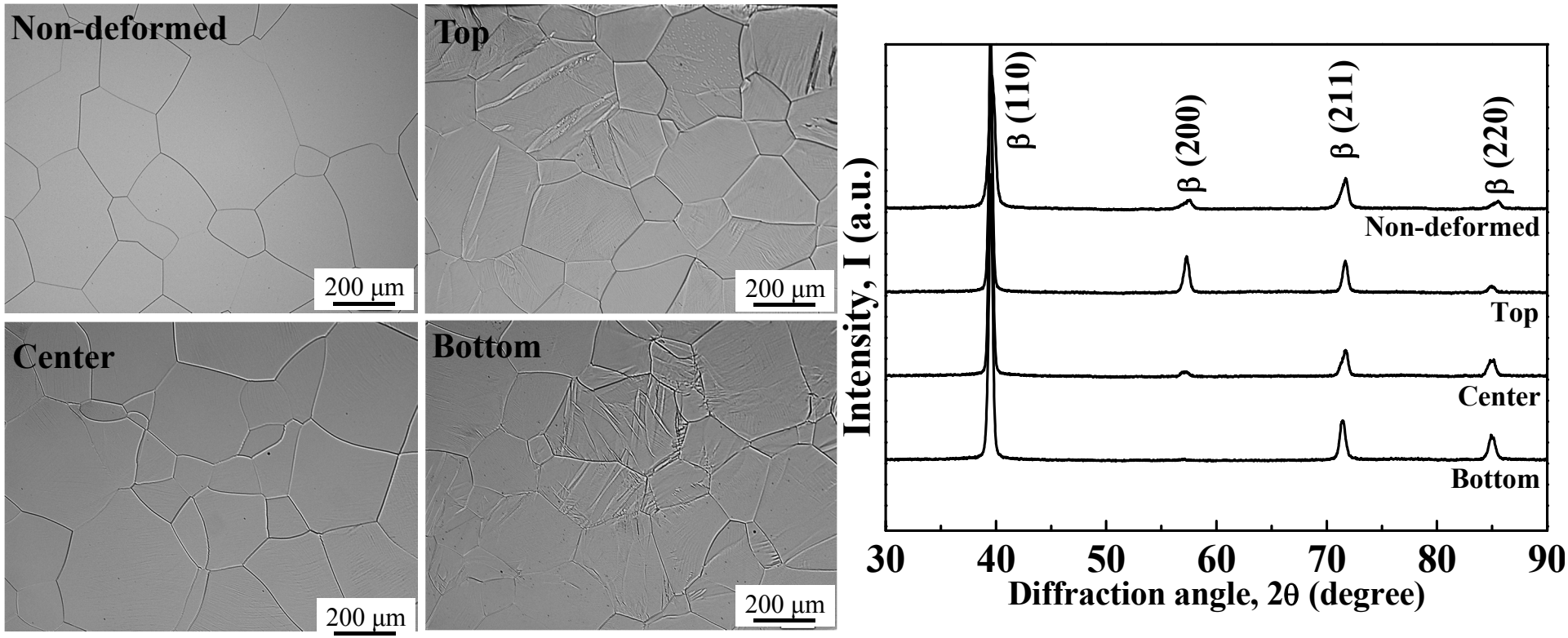

Fig. 4. Optical micrographs and XRD profiles of non-deformed and deformed parts of Ti-12Cr subjected to bending deformation (after bending test with 4 mm deflection).

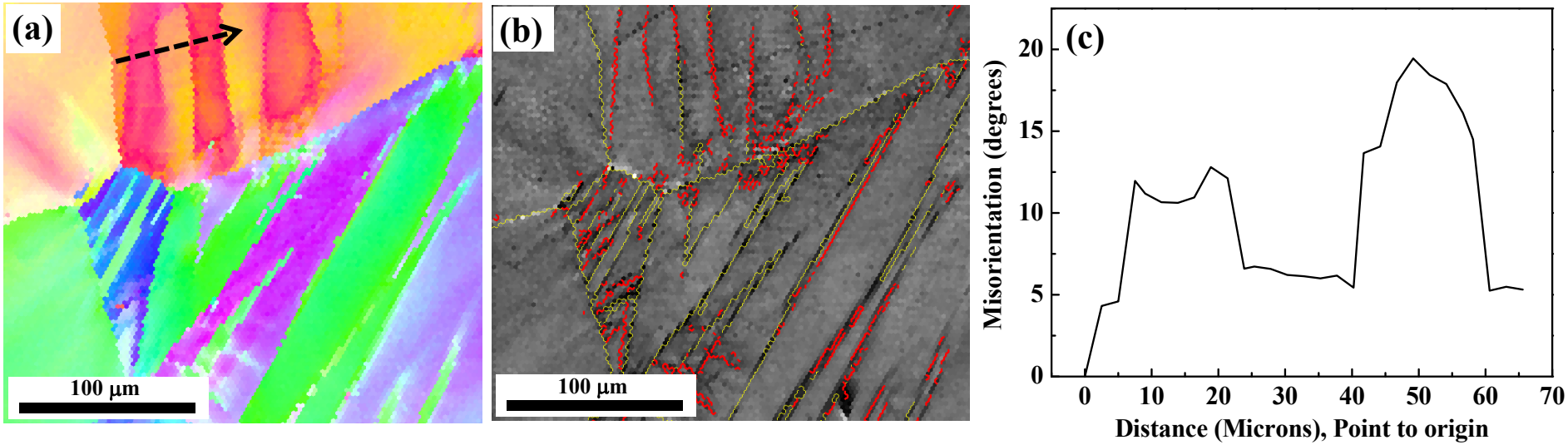

Fig. 5. EBSD analysis of tension area of bending deformed Ti-12Cr (after bending test with 4 mm deflection): (a) local orientation image map (OIM), (b) grain boundary map showing boundaries with a misorientation of ~10° along the <110>β direction (red lines), (c) misorientations relative to the first point along black arrows in (a).

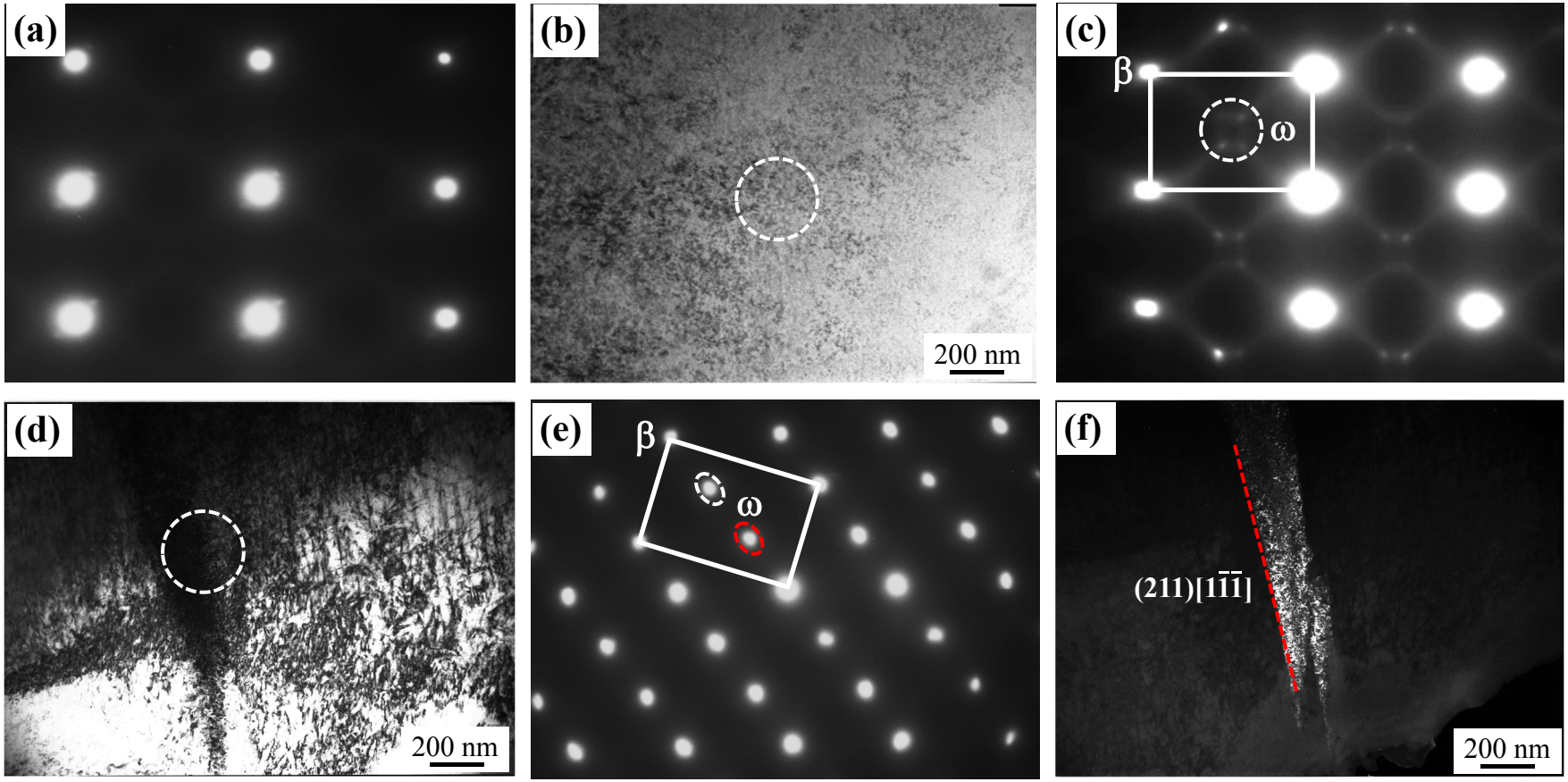

Fig. 6. TEM observations of (a) non-deformed and (b-f) deformed parts of bent Ti-12Cr (after bending test with 4 mm deflection): (a) selected area electron diffraction pattern (SAED) of non-deformed part; (b) bright field image of compression area; (c) SAED taken from part marked by circle in (b); (d) bright field image of tension area; (e) SAED taken from area labeled by circle in (d); (f) dark field image corresponding to diffraction spot denoted by red circle in (e). The beam direction is parallel to [110] β direction.

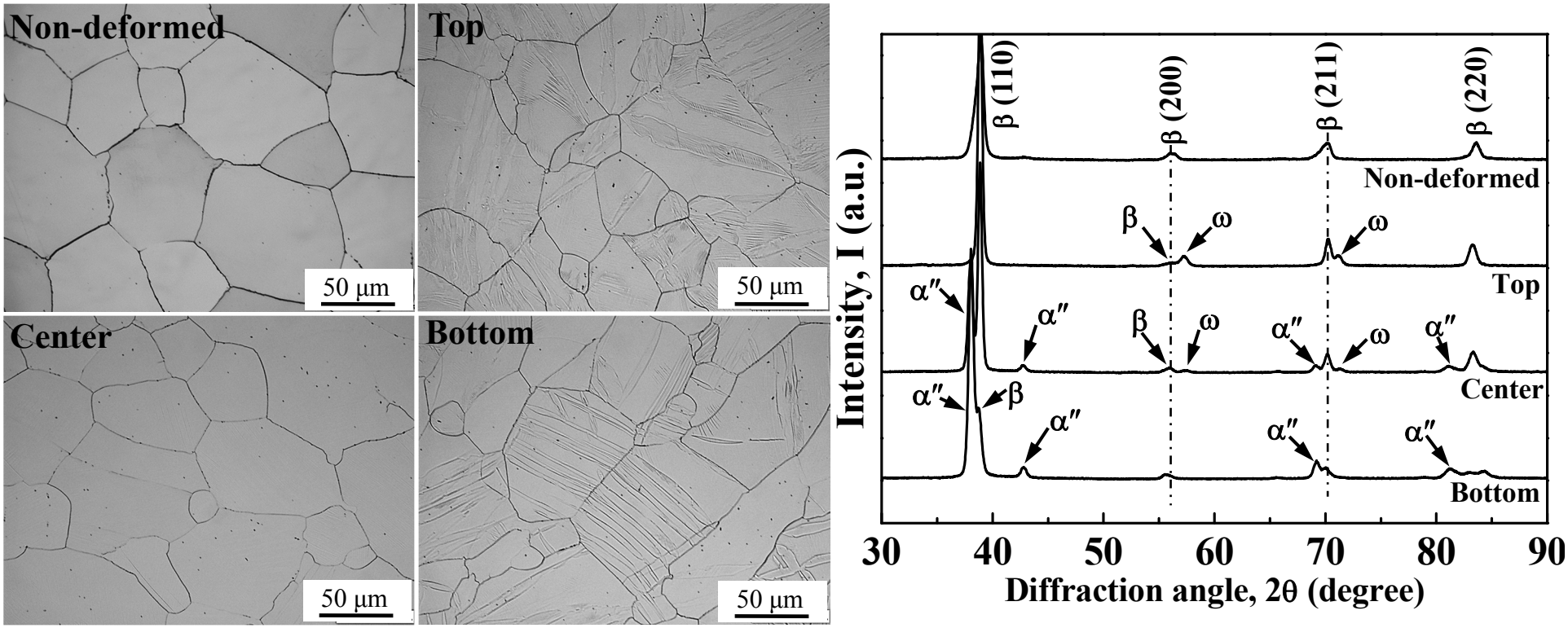

Fig. 7. Optical micrographs and XRD profiles of non-deformed and deformed parts of TNTZ subjected to bending deformation (after bending test with 4 mm deflection).

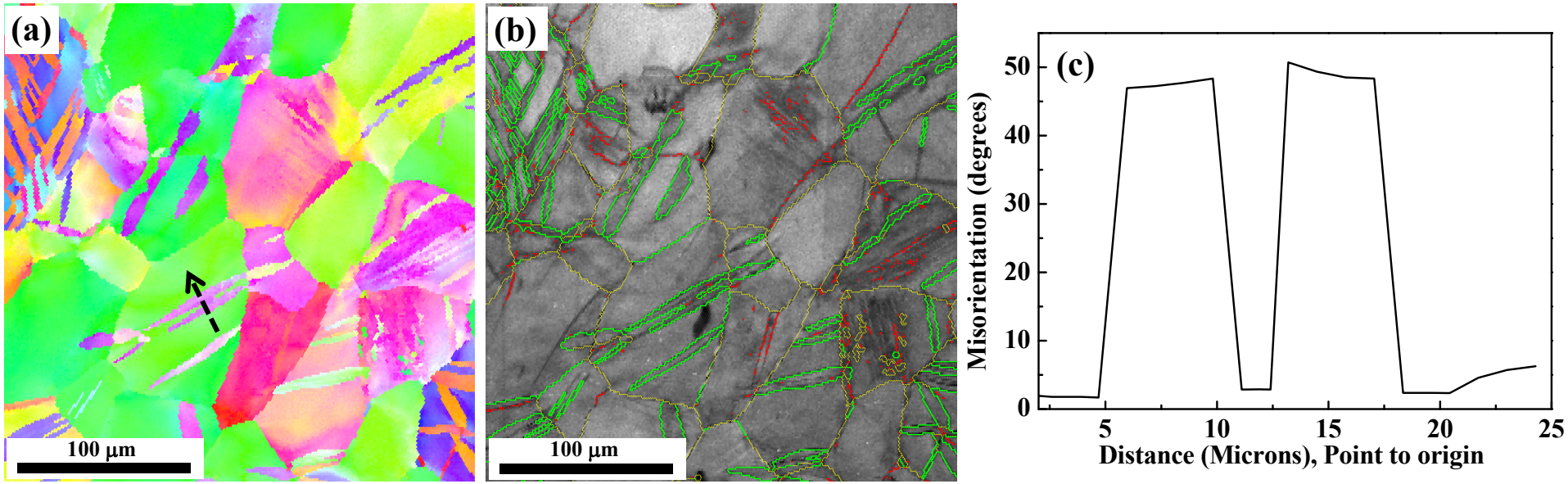

Fig. 8. EBSD analysis of tension area of bending deformed TNTZ (after bending test with 4 mm deflection): (a) local orientation image map (OIM), (b) grain boundary map showing boundaries with a misorientation of ~50.5° along <110>β direction (green lines), (c) misorientations relative to the first point along black arrows in (a).

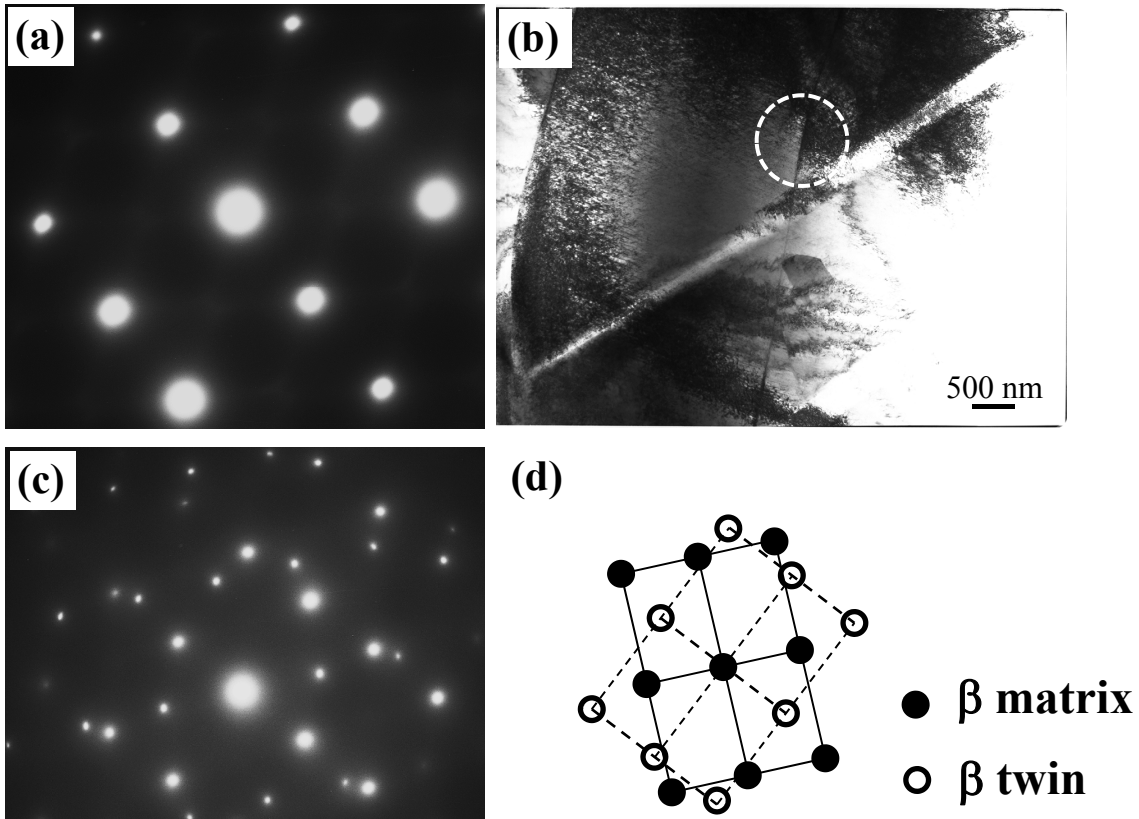
(a)
(b)
500 nm
(c)
(d)
β matrix
β twin

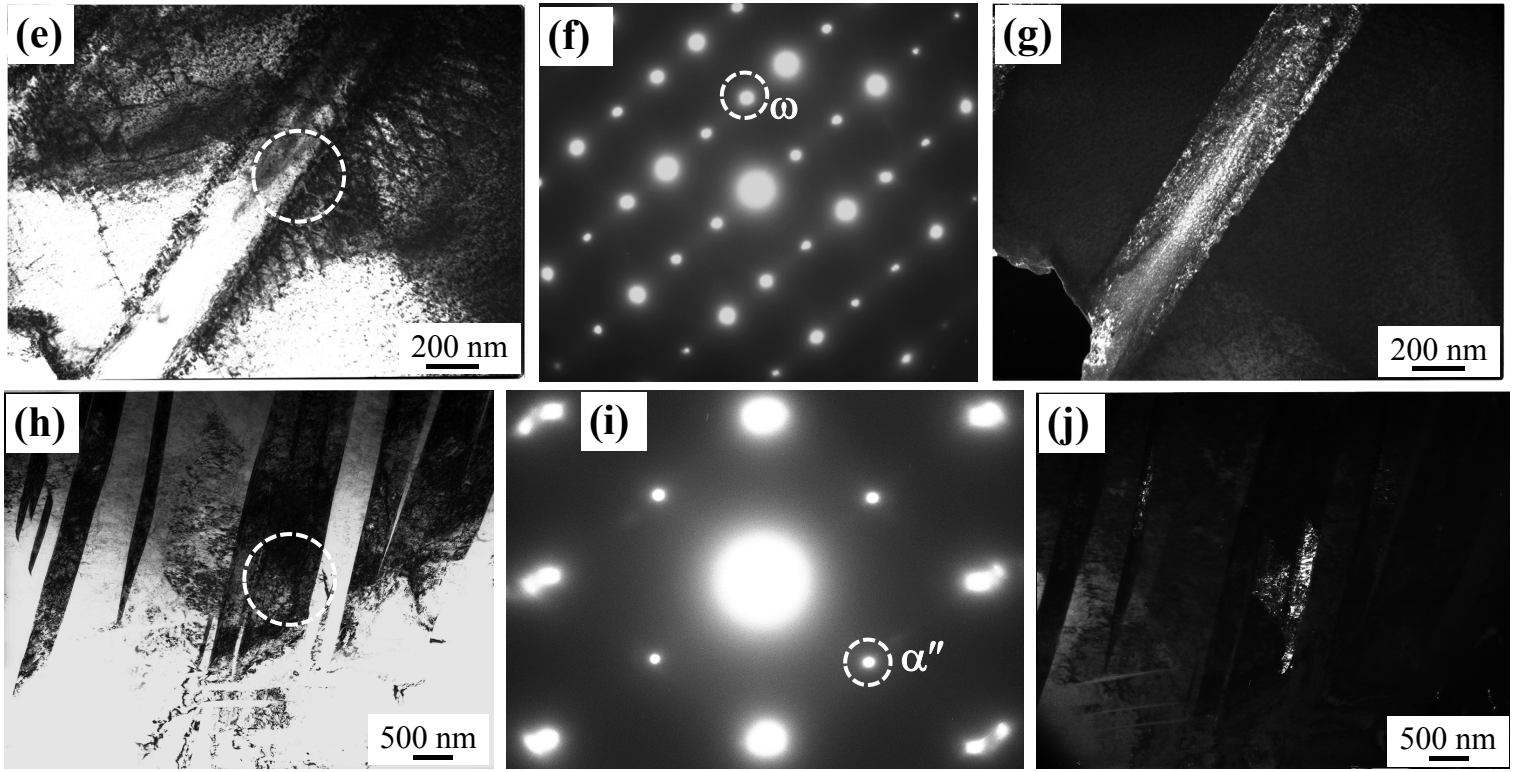

Fig. 9. TEM observations of non-deformed part (a), compression area (b-g) and tension area (h-j) of deformed part of bended TNTZ (after bending test with 4 mm deflection): (a) selected area electron diffraction pattern (SAED) of non-deformed part; (b) bright field image of compression area; (c) SAED taken from part marked by circle in (b); (d) corresponding key diagram; (e) bright field image of compression area; (f) selected area electron diffraction pattern (SAED) taken from part marked by circle in (e); (g) dark field image corresponding to diffraction spot denoted by circle in (f); (h) bright field image of tension area; (i) SAED taken from part marked by circle in (h); (j) dark field image corresponding to diffraction spot denoted by circle in (i). The beam direction is parallel to [110]β direction.

Graphical Abstract